



# Vanadium-phosphorus incorporation induced interfacial modification on cobalt catalyst and its super electrocatalysis for water splitting in alkaline media

Zizheng Zhu<sup>a</sup>, Kai Xu<sup>a</sup>, Wen Guo<sup>a</sup>, Hongyan Zhang<sup>a</sup>, Xin Xiao<sup>a</sup>, Maoshuai He<sup>b</sup>, Tingting Yu<sup>a</sup>, Hong Zhao<sup>a</sup>, Dongen Zhang<sup>a</sup>, Tao Yang<sup>a,\*</sup>

<sup>a</sup> School of Environmental and Chemical Engineering, Jiangsu Ocean University, Lianyungang 222005, China

<sup>b</sup> Key Laboratory of Eco-Chemical Engineering, Ministry of Education, College of Chemistry and Molecular Engineering, Qingdao University of Science and Technology, Qingdao 266042 China

## ARTICLE INFO

### Keywords:

Water splitting  
Electrocatalyst  
Vanadium  
Cobalt  
Metalloid

## ABSTRACT

Co-based compounds have been considered as promising earth-abundant electrocatalysts for water splitting, however, the catalytic performance need to be further enhanced. Herein, we report a nickel foam (NF) supported Co-VOx-P nanoflower electrocatalyst that shows excellent catalytic performances, achieving a small overpotential of 230 mV at 100 mA/cm<sup>2</sup> for OER. Such performances surpass the recently reported best-performing Co-based catalysts in alkaline media. In addition, the present Co-VOx-P electrocatalyst can deliver 10 mA/cm<sup>2</sup> with a small overpotential of 98 mV for HER. Experimental and DFT studies indicate that, due to the combination of P and V, the Co-VOx-P electrocatalyst shows improved intrinsic catalytic properties including enhanced conductivity, facile electron transfer and favorable surface adsorption strength. The strategy demonstrated here by incorporating metalloid with high valence states may be extended to design other cost-efficient electrocatalysts for more advanced water splitting performances.

## 1. Introduction

The ever-increasing concerns over energy sources and environment have driven considerable efforts for sustainable and clean energy technologies [1]. Hydrogen energy, characterized by high energy density, renewability and clean, is nowadays known as an ideal alternative energy carrier [2]. Electrochemical water splitting has become one of the most prospective strategies for hydrogen generation, which involves hydrogen evolution reaction (HER) and oxygen evolution reaction (OER) [3]. Due to the sluggish multi-transfer of proton-coupled electron, remarkable overpotentials are now required, especially for OER [4]. To date, the benchmark electrocatalysts towards HER and OER are generally noble metals such as Pt, Ir and Ru, but suffer from relative scarcity and high cost [5–7]. Great efforts have been focused on first-row transition metals as alternative catalysts. However, most of the transition metal based catalysts cannot compete with the aforementioned noble metals [8–11].

Recently, earth-abundant Co-based compounds such as oxides, hydroxides and phosphides have been studied as efficient water splitting

catalysts [12–16]. Especially, the metalloid Co-based phosphide outperformed the corresponding oxide/hydroxide, which has been recognized as one of the most active catalysts due to the low overpotential and the high evolution current [14,17]. The phosphides display great improvements in structure and composition. More active catalytic sites originated from the surface roughening and structural reconstruction during the synthesis of Co-P catalysts. The in situ formed metal-oxo/hydroxo species during the electrochemical processes were also believed to contribute to the enhanced performance [18,19]. More importantly, the surface electronic structure and the adsorption properties of Co sites can be efficiently modified. Although the in-depth molecular-level understanding of the sluggish electrochemical steps taking place on metal phosphides remains ambiguous, the active sites are commonly recognized as the metal-cation of Co. Thereafter, the chemical environment of Co should be highly important for the high OER catalysis. Due to the difference in electronegativities, the electrons may transfer from Co atoms to P atoms and thereby promotes the formation of high-valence metal species with higher oxidizing power. The local electrostatic interactions between metal cations and OH<sup>-</sup> groups

\* Corresponding author.

E-mail address: [yangtao\\_hit@163.com](mailto:yangtao_hit@163.com) (T. Yang).

<https://doi.org/10.1016/j.apcatb.2021.120985>

Received 9 October 2021; Received in revised form 7 November 2021; Accepted 28 November 2021

Available online 3 December 2021

0926-3373/© 2021 Elsevier B.V. All rights reserved.

are then enhanced, which leads to faster electrochemical kinetics, especially for the OER process [16]. Even so, phosphides still require a large overpotential of 200–300 mV to reach the OER current density of 10 mA/cm<sup>2</sup> in concentrated alkaline media (e.g. 1.0 M KOH) [20,21]. This catalytic performance is still less than satisfactory, especially at a higher electrolysis current density.

How about adding another electrophilic element into phosphides to furtherly tune the electronic state of the metal active sites? The latest work showed that non-metal element S can be used to enhance the water splitting performance, especially for OER [22–24]. However, the conductivity and the stability are short of expectation that limiting the further improvement and industrial applications.

Recently, vanadium-based compounds, with superior conductivity and strong metallic properties, have been considered as up-and-coming star materials for HER [25–27] and OER [28–30]. For the oxygen evolution process in alkaline media, the reaction from \*OH to \*OOH shows a large energy barrier. The high valences of vanadium with strong electrophilicity can draw electrons from the neighboring metal ions and accelerate the reaction of \*OH with the adsorbed O to form \*OOH [31, 32]. A vanadium doped Co-P nanoparticle was recently reported as an efficient catalyst for water splitting, requiring overpotentials of 235 mV and 340 mV for the electrolysis current density of 10 mA/cm<sup>2</sup> towards HER and OER, respectively [33]. However, the catalytic activity needs further improvement and the insight for the promising enhancement and electronic synergy at the atomic level should be investigated in depth.

Herein, we synthesized a ternary Co-V-P catalyst with a nanoflower structure directly onto the Ni foam via a facile two-step method. By the combination of V and P, the Co-VOx-P demonstrated excellent catalytic performance for both HER and OER under alkaline environment. The detailed electrochemical measurements showed that a small overpotential of 98 mV was required to reach the HER current density of 10 mA/cm<sup>2</sup> and afforded a low Tafel slope of 59 mV/dec, a small overpotential of 230 mV was required for delivering the OER current density of 100 mA/cm<sup>2</sup> and afforded a very low Tafel slope of 64 mV/dec. The vanadium incorporation can improve the electronic conductivity of the active material, and enhance catalytic performance, which was furtherly revealed by density functional theory (DFT) analysis.

## 2. Experimental

### 2.1. Materials

Nickel foam (NF) was obtained from Guangshengjia New Materials Co., Ltd. Ammonium vanadate (NH<sub>4</sub>VO<sub>3</sub>) and cobalt chloride hexahydrate (CoCl<sub>2</sub>·6H<sub>2</sub>O) were purchased from Aladdin Industrial Corporation, all chemicals were used as purchased without pretreatment.

### 2.2. Synthesis of the self-supported Co-VOx-P catalyst on Ni foam

The synthesis of self-supported Co-VOx-P on Ni foam involved two steps, a hydrothermal reaction and a phosphorization in the gas phase. Before the preparation, the Ni foam with an area of 2 cm × 3 cm was washed with the assistance of sonication in 3 M HCl (30 min), acetone (8 min), ethanol and deionized water (10 min) consecutively, and then used as a substrate. NH<sub>4</sub>VO<sub>3</sub> (0.5 mmol), CoCl<sub>2</sub>·6H<sub>2</sub>O (1 mmol) were dispersed in deionized water (30 mL) with magnetical stirring at 45 °C until a transparent pink solution was prepared. The as-obtained solution was then put into a 50 mL Teflon-lined autoclave with one piece of pretreated Ni foam. The autoclave was sealed, and kept at 180 °C. After 12 h, the autoclave was cooled to room temperature, the Ni foam was dried at 70 °C for 4 h. Then the NF was put into a porcelain boat, 1 g NaH<sub>2</sub>PO<sub>2</sub> was also put in the boat upstream. In a tube furnace, the boat was heated to 300 °C at a heating rate of 5 °C min<sup>-1</sup> under Ar atmosphere. After maintaining 300 °C for 50 min, the furnace was cooled to room temperature.

For comparison, a self-supported Co-P on NF was synthesized without using NH<sub>4</sub>VO<sub>3</sub>, and a self-supported Co-VOx on NF was synthesized through the hydrothermal process.

The commercial catalysts, such as Pt/C, IrO<sub>2</sub> and RuO<sub>2</sub>, were loaded onto NF through the following method. A mixed solution containing 260 μL ethanol, 90 μL Nafion (5 wt%) and 650 μL deionized water was firstly prepared. 25 mg commercial catalysts were then put into the above solution and dispersed with the assistance of sonication until a uniform ink was achieved. 100 μL of the catalyst ink was dropped onto the Ni foam, that was dried in airflow for use.

### 2.3. Structural characterization

The crystal structures of the as-prepared electrocatalyst were demonstrated with powder X-ray diffraction (XRD) conducted on a Bruker D8 Advance X-ray diffractometer (Cu Kα radiation, 40 kV, 40 mA). X-ray photoelectron spectroscopy (XPS) test was performed on a Thermo Scientific K-Alpha XPS instrument. Transmission electron microscopy (TEM), high-resolution transmission electron microscopy (HRTEM), energy-dispersive X-ray spectroscopy (EDS) and corresponding elemental distribution were obtained on a FEI Tecnai G2 F30.

### 2.4. Electrochemical measurements

All the electrochemical experiments were carried out in 1.0 M KOH on an Autolab potentiostat/galvanostat (PGSTAT-302N) workstation at room temperature. A typical three-electrode cell system with catalyst working electrodes, graphite rod counter electrode and Hg/HgO reference electrode was used. Before each measurement, the electrolyte was bubbled for 30 min with high-purity Ar. The linear sweep voltammetry (LSV) curves were performed in 1.0 M KOH, and 20 cycles of cyclic voltammetry (CV) tests were operated before the measurements for activation. All applied potentials were switched with respect to the reversible hydrogen electrode (RHE) based on the following equation: E (V vs. RHE) = E (V vs. Hg/HgO) + 0.0591 pH + 0.098.

For HER measures, the LSVs were subsequently performed with a scan rate of 5 mV s<sup>-1</sup>. As for the OER tests, the LSVs were subsequently carried out with a scan rate of 10 mV s<sup>-1</sup>. Chronoamperometry was used to evaluate the durability by detecting the change of current density at a certain overpotential. To investigate the electrochemical active surface areas (EASAs), CVs were conducted at different scanning rates (20, 40, 60, 80, 100 mV s<sup>-1</sup>). The electrochemical double-layer capacitance (C<sub>dl</sub>) was calculated from the CVs data. Electrochemical impedance spectroscopy (EIS) measurements were carried out in the frequency region of 0.01–10<sup>5</sup> Hz with an AC amplitude of 5 mV.

### 2.5. DFT calculation

The stability evaluation of Co-Vox-P and the geometry/electronic structures optimization were performed using the Vienna Ab-initio Simulation Package (VASP) [34,35] according to the experimental results of XRD, XPS and TEM characterizations. Cut-off energy of 450 eV was set in our calculation, and 3 × 3 × 1 Monkhorst-Pack k grids were applied during the optimization. The generalized gradient approximation (GGA) was used to describe the exchange-correlation interactions [36] in the form of the Perdew-Burke-Ernzerhof functional (PBE) [37]. DFT+D3 method was performed to describe the weak interaction with empirical correction in Grimme's scheme [38]. To avoid the interaction between periodical images, we built four-layer Co<sub>2</sub>P (211) slab with vacuum layer 15 Å. The reaction Gibbs free energy changes (ΔG) for each elementary step were calculated and used as a descriptor for the theoretical overpotentials. The detailed DFT calculation was presented in [Supporting information](#).

### 3. Results and discussion

#### 3.1. Characterization of Co-VOx-P electrocatalyst

The synthesis process of the Co-VOx-P electrocatalyst was displayed in Fig. 1A. The Co-VOx nanoflowers were synthesized onto Ni foam directly via a facile hydrothermal process under optimized temperature and time, in which,  $\text{CoCl}_2$  and  $\text{NH}_4\text{VO}_3$  were used as precursors. After the hydrothermal reaction, the surface of Ni foam was covered with a brown film suggesting the success in forming Co-VOx compounds. The Ni foam supported Co-VOx was then reacted with  $\text{NaH}_2\text{PO}_4$  in a gas-phase reaction. Scanning electron microscopic (SEM) images of the product clearly show that the entire surface of Ni foam was uniformly coated with the densely interlaced nanoflowers (Figs. 1B, C), which is very different from the smooth surface of the pristine Ni foam (Fig. S1, S2). A close inspection in Fig. 1D reveals that the interlaced nanoflowers were assembled by many interconnected plate-like petals with rough surfaces, with a lateral size of few hundreds of nanometers and a thickness of few tens of nanometers. Such 3D open nanoarchitecture built by hierarchical nanoflowers and nano-plates would provide more active catalytic sites and fast diffusion of electrolyte, to enhance the water electrolysis activity. These SEM results suggest that a favorable hierarchical nano-structural electrode for solution catalytic reaction was successfully generated. It is interesting that no product can be generated without using Ni foam in the hydrothermal process (Figure Sx). In our point of view, in presence of Ni foam, the Ni surface acted as both

substrate and catalyst for deposition. For comparison, a quite different rough Co-P surface with micro-pores on Ni foam was prepared through the two-step method (Fig. S3). Co-VOx was synthesized onto Ni foam through the same hydrothermal process, showing a similar nano-structure to that one of Co-VOx-P (Fig. S4). The structure inheriting from Co-VOx to Co-VOx-P indicated that the gas-phase phosphorization reaction cannot break or destroy the Co-VOx structure. The composition and elemental distribution were quantitatively illustrated by SEM-energy dispersive X-ray (SEM-EDX) and transmission electron microscopy-EDX (TEM-EDX) (Fig. 1E) on different scales. SEM-EDX spectra showed the presence of Co, P and V in the samples. The atom ratio of Co/P/V on nanoflowers in SEM images is 49/20/31 (Fig. S5, S6), on a petal in TEM is 53/21/26 (Fig. S7). All the elements of Co, O, V and P were distributed homogeneously on the samples (Fig. S8, S9 and Fig. 1E). X-ray diffraction (XRD) was employed to disclose the crystal structure and composition of the as-synthesized samples. The strong diffraction peaks at  $44.37^\circ$ ,  $51.60^\circ$ ,  $76.08^\circ$  and  $92.10^\circ$  could be assigned to (111), (200), (220) and (311) planes of face-centered cubic Ni (PDF#01-1258). Expect for the distinct Ni reflections, XRD patterns showed very weak peaks, indicating that the products synthesized through our processes are amorphous or weakly crystallized. The weak peaks at  $41.02^\circ$ ,  $41.78^\circ$  and  $48.96^\circ$  should be attributed to the planes of (112), (210) and (013) of  $\text{Co}_2\text{P}$  with some contraction (Fig. S10). The petals were peeled off with the assistance of ultrasonication and tested by TEM to reveal the defined nanostructure. The TEM image shown in Fig. S11 suggested that the petals were composed of many small

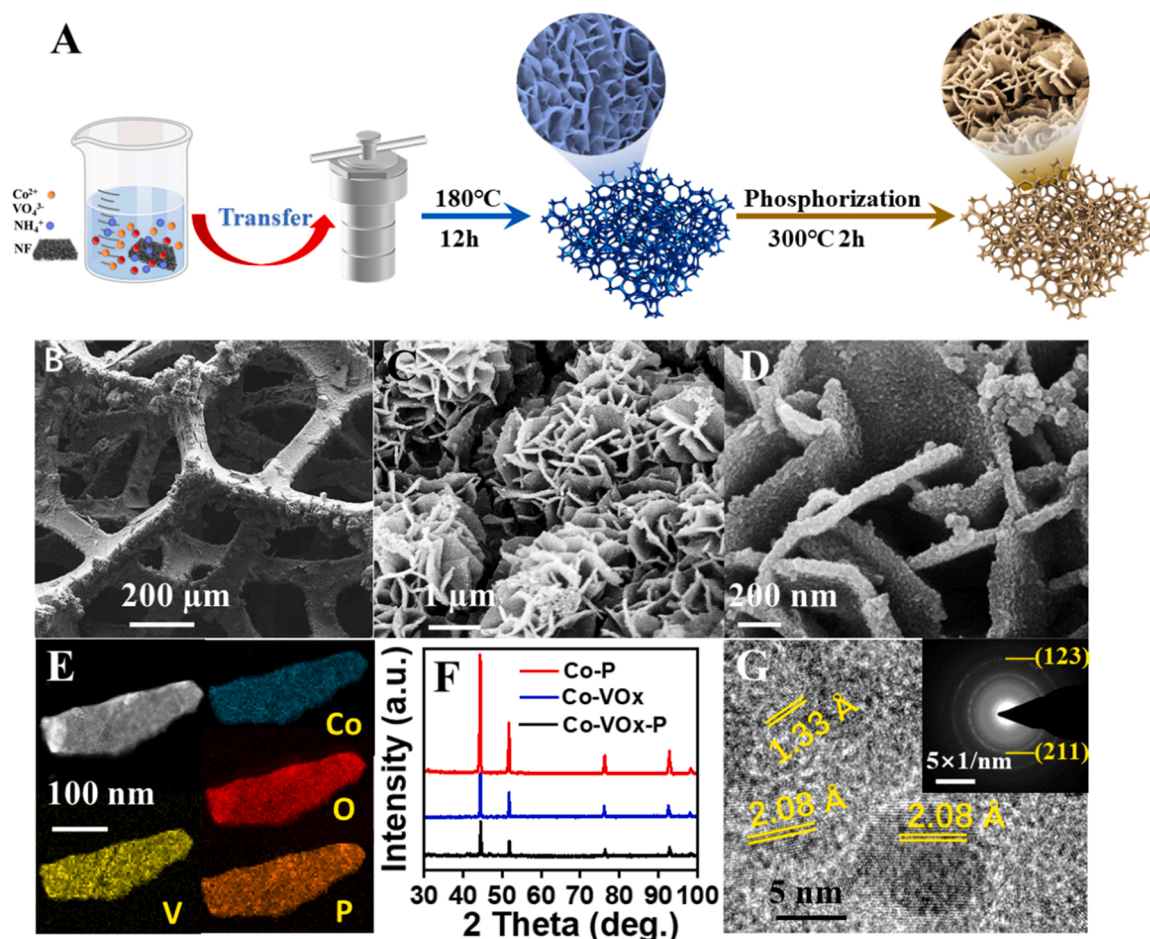


**Fig. 1.** Structural characterization of Co-VOx-P. (A) Schematic view of the synthesis processes of Co-VOx-P on Ni foam. (B) SEM image of the Ni foam framework coated by Co-VOx-P. (C) SEM image of nanoflower-like Co-VOx-P on Ni foam surface. (D) SEM image of plate-like Co-VOx-petals (E) HAADF-STEM image and the corresponding elemental mapping of Co, V, O and P. (F) XRD patterns of Co-VOx-P, Co-VOx and Co-P. (G) HRTEM image of Co-VOx-P and the corresponding SAED pattern.



particles (3–5 nm). HRTEM in Fig. 1G revealed the lattice spacing of 2.08 Å and 1.33 Å, assigning to the planes of (211) and (123) for Co<sub>2</sub>P. The inset in Fig. 1G displayed the selected area electron diffraction (SAED) patterns of Co-VOx-P petal, characterized by the distinct diffraction rings of (211) and (123) lattices for Co-P, which was highly consistent with the HRTEM results.

X-ray photoelectron spectroscopy (XPS) was then carried out for an insight of the electronic interaction between P/V and Co at the atomic level in the near-surface region. The XPS survey spectra clearly illustrated the existence of Co (810–775 eV), V (530–510 eV), P (140–130 eV) and O (535–530 eV), which were consistent with the results of EDX (Fig. S12). For comparison, a VOx was directly grown onto NF through the same hydrothermal method. Fig. 2 shows the comparison of Co 2p and V 2p XPS core-level spectra of the Co-VOx-P, Co-VOx, Co-P and VOx, suggesting the strong electron synergism effect in the surface region. The high-resolution Co 2p spectra showed two peaks corresponding to Co 2p<sub>3/2</sub> (780–782 eV) and Co 2p<sub>1/2</sub> (796–799 eV), attributing to the spin-orbit splitting of the p orbital along with two shakeup satellites, respectively. Compared with Co-P (780.38 eV) and Co-VOx (781.78 eV), the binding energy of Co in Co-VOx-P (783.16) showed some increase, suggesting the chemical environment of Co was greatly changed by the co-incorporation of P and V. The core-level spectrum of V 2p can be decomposed as V 2p<sub>3/2</sub> (517–515 eV) and V 2p<sub>1/2</sub> (526–523 eV). Each of them can be deconvoluted as three sub-peaks of V (III), V(VI) and V(V) species, indicating that V atoms are dominantly in high oxidation states [39]. The percent of V(V) in Co-VOx-P (516.88 eV) is much lower than that of Co-VOx (517.28 eV) and VOx (517.58), suggesting an electron transfer from Co to V. Due to the difference in radii, some of the vanadium at high oxidation states would exist at the surface as VOx [40]. The fitting peak of O1s in Fig. S13 showed three peaks at 530.9 eV corresponding to metal-O bond, 531.6 eV assigning to V-O bond and 532.7 eV ascribing to oxygen species in the surface adsorbed water molecule [41]. It should be noted that Co 2p binding energy for the Co-VOx-P shifted obviously to a higher

position in contrast to Co-P. On the other contrary, the V 2p peaks shifted to a lower binding energy in Co-VOx-P and Co-VOx compared to that one of VOx. These binding energy shifts suggested a partial electron transfer from Co to V between metal ions, which is in good agreement with the previous work [42]. The XPS peaks at 133–134 eV should be assigned to the POx in Co-VOx-P and Co-P (Fig. S14).

### 3.2. Electrochemical hydrogen evolution performance of Co-VOx-P catalyst

The electrochemical HER activities were evaluated in a typical three-electrode system with a graphite counter electrode, a HgO reference electrode and a catalyst working electrode. Linear sweep voltammetry (LSV) was recorded in Ar saturated 1.0 M KOH electrolyte with a negative scanning rate of 5 mV s<sup>-1</sup>. At the same time, commercial Pt/C (20 wt%) was loaded onto Ni foam and measured under the same condition for benchmark. Fig. 3A displayed the HER polarization curves of the catalytic samples. Bare Ni foam has bare catalysis for HER in alkaline media. The commercial Pt/C reached an onset HER potential close to zero [43]. Compared with Co-VOx and Co-P, Co-VOx-P achieved the best catalytic performance with the highest catalytic current density and the lowest overpotential. To deliver a typical current density of 10 mA/cm<sup>2</sup>, Co-VOx-P required a low overpotential of 98 mV, which is much lower compared to Co-P (201 mV) and Co-VOx (160 mV) (Fig. 3B).

Additionally, the current densities on Co-VOx-P increased sharply with the overpotential. For example, to reach the large HER current density of 50 mA/cm<sup>2</sup>, Co-VOx-P required an overpotential of 140 mV. In comparison, Co-P and Co-VOx needed the overpotential of 250 mV and 200 mV to obtain the same current density, respectively. The small overpotentials for large current densities suggested a remarkable application. The durability test was performed by successive potential cycling at the HER polarization range. Fig. 3C revealed that Co-VOx-P showed a good stability and bare attenuation could be observed in LSV curves after the successive potential cycling. The durability was also

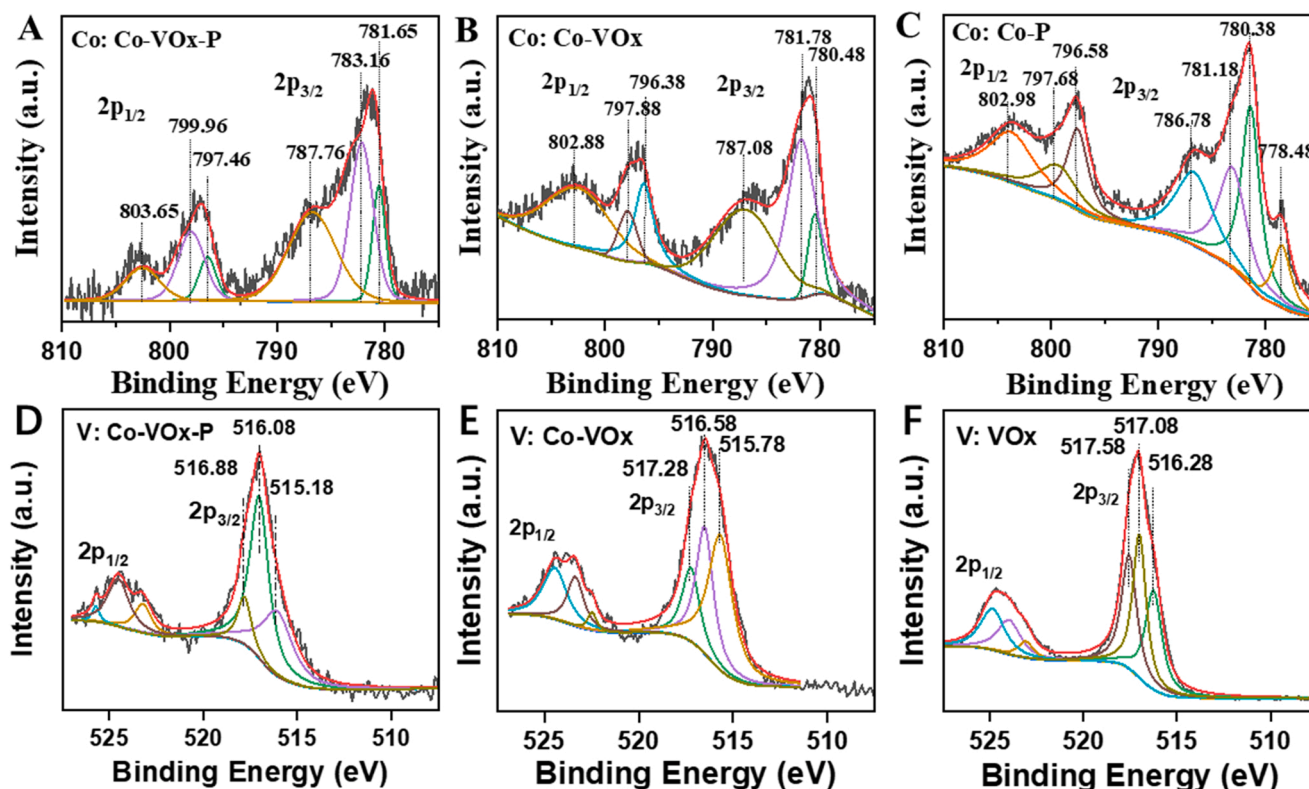
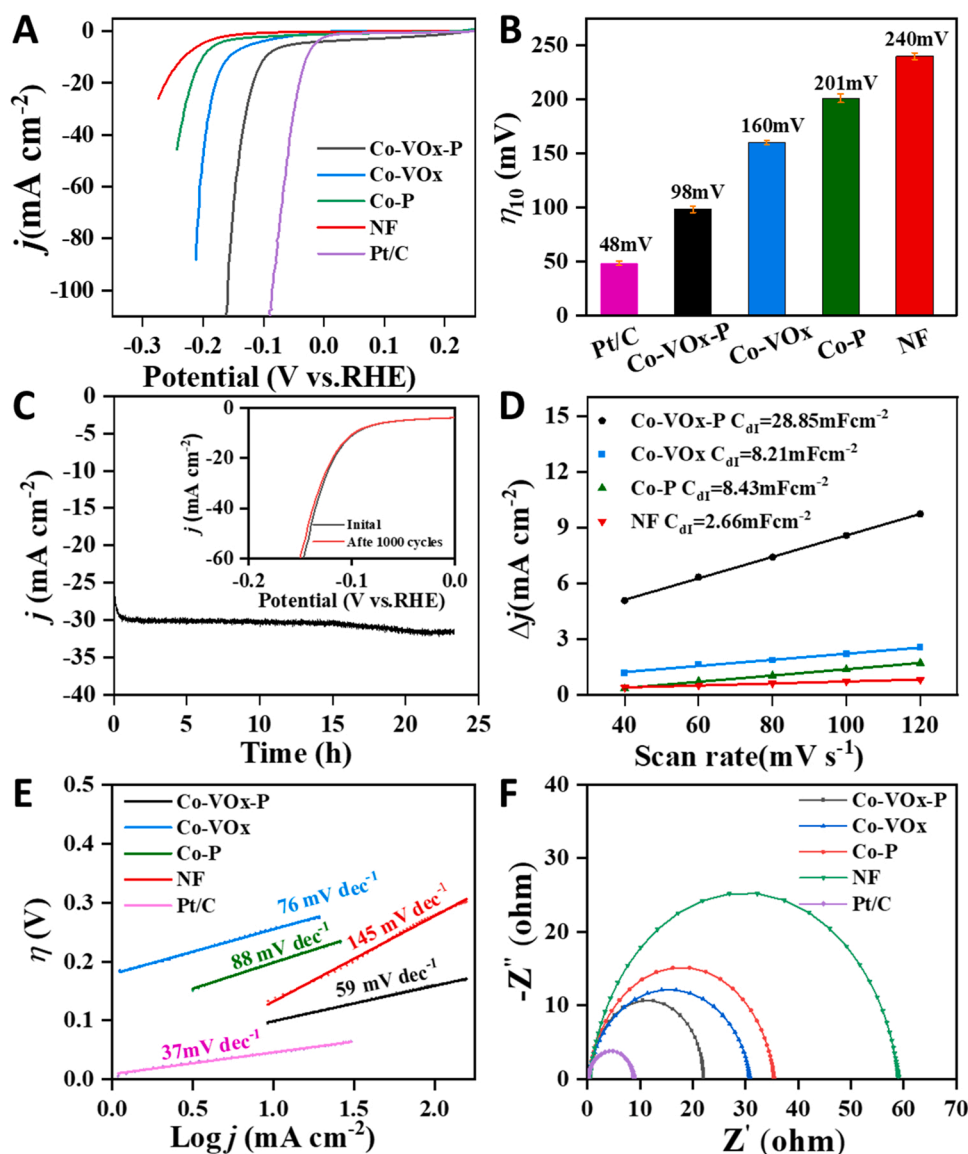


Fig. 2. High-resolution XPS spectra of Co in (A) Co-VOx-P, (B) Co-VOx and (C) Co-P, High-resolution XPS spectra of V in (D) Co-VOx-P, (E) Co-VOx and (F) VOx.



**Fig. 3.** Electrochemical measurements. (A) HER polarization curves of Co-VOx-P, Co-VOx, Co-P, bare Ni foam (NF) and commercial Pt/C catalysts in 1.0 M KOH. (B) The comparison of overpotential for delivering 10 mA/cm<sup>2</sup> HER current density. (C) Stability test of Co-VOx-P catalyst through the method of successive potential cycling and long-term operation. (D)  $C_{dl}$  of the Co-VOx-P, Co-VOx, Co-P and NF. (E) Tafel slopes of Co-VOx-P, Co-VOx, Co-P, NF and commercial Pt/C catalysts. (F) EIS spectra of Co-VOx-P, Co-VOx, Co-P, NF and commercial Pt/C catalysts.

tested by the chronoamperometry method. At an overpotential of 130 mV, the current density was stable at 30 mA/cm<sup>2</sup> and even increased up to 31.9 mA/cm<sup>2</sup> after 24 h. The slight increase of the HER electrolysis current density also appeared in other V contained electrocatalysts [43].

To gain an insight to the high catalytic performance, electrochemical active surface area (EASA) was analyzed, which was calculated by  $C_{dl}$  obtained from the cyclic voltammetry (CV) profiles with different scanning rates (Fig. 3D, Fig. S15). Co-VOx-P displayed the largest EASA, nearly 3.5 times that of Co-VOx, and Co-P, indicating that the catalysis enhancement should partly be attributed to the large active area. Nevertheless, it is important to note that the high catalytic activity should not be merely relative to the large active area. At an overpotential of 160 mV, the electrolysis current density of Co-VOx-P was as high as 105 mA/cm<sup>2</sup>, which was ten times and thirty times higher than those of Co-VOx (10 mA/cm<sup>2</sup>) and Co-P (3.5 mA/cm<sup>2</sup>), respectively. These results suggested that Co-VOx-P may have higher intrinsic catalytic activity for hydrogen evolution. The intrinsic activity of catalysts can be reflected by the onset potential and Tafel slope, which were controlled by the type of active sites rather than its morphology, quantity and surface area [28,44]. As shown in Fig. 3E, Co-VOx-P displayed a sharper onset evolution current density at relatively lower

overpotential, implying the facile kinetics for hydrogen evolution. Tafel slopes of Co-VOx, Co-P and Co-VOx-P are smaller than Volmer (118.2 mV dec<sup>-1</sup>) and higher than Heyrovsky (39.4 mV dec<sup>-1</sup>), indicating a Volmer-Heyrovsky mechanism [22]. Except for the commercial Pt/C of 37 mV dec<sup>-1</sup>, Co-VOx-P displayed the smallest slope of 59 mV dec<sup>-1</sup>, indicating the superior type of the active sites and a higher catalytic activity. The better intrinsic activity of Co-VOx-P may be due to the high conductivity, which was verified by electrochemical impedance spectroscopy (EIS). The Nyquist profiles of all the samples showed distinct semicircles with different diameters at the high-frequency regions, which should be mainly ascribed to the resistance of charge transfer (Fig. 3F). The semicircle of Co-VOx-P showed the smallest diameter, suggesting the lowest resistance for charge transfer, that is, the highest conductivity, highly in agreement with the Tafel slopes analysis. Performance of the present Co-VOx-P has been compared with the recently reported HER catalysts (Table S1).

### 3.3. Electrochemical oxygen evolution performance of Co-VOx-P catalyst

The OER performance was also determined in 1.0 M KOH electrolyte. The commercial IrO<sub>2</sub> and RuO<sub>2</sub> were loaded on Ni foam and also tested in the same condition. Fig. 4A showed the polarization curve of the

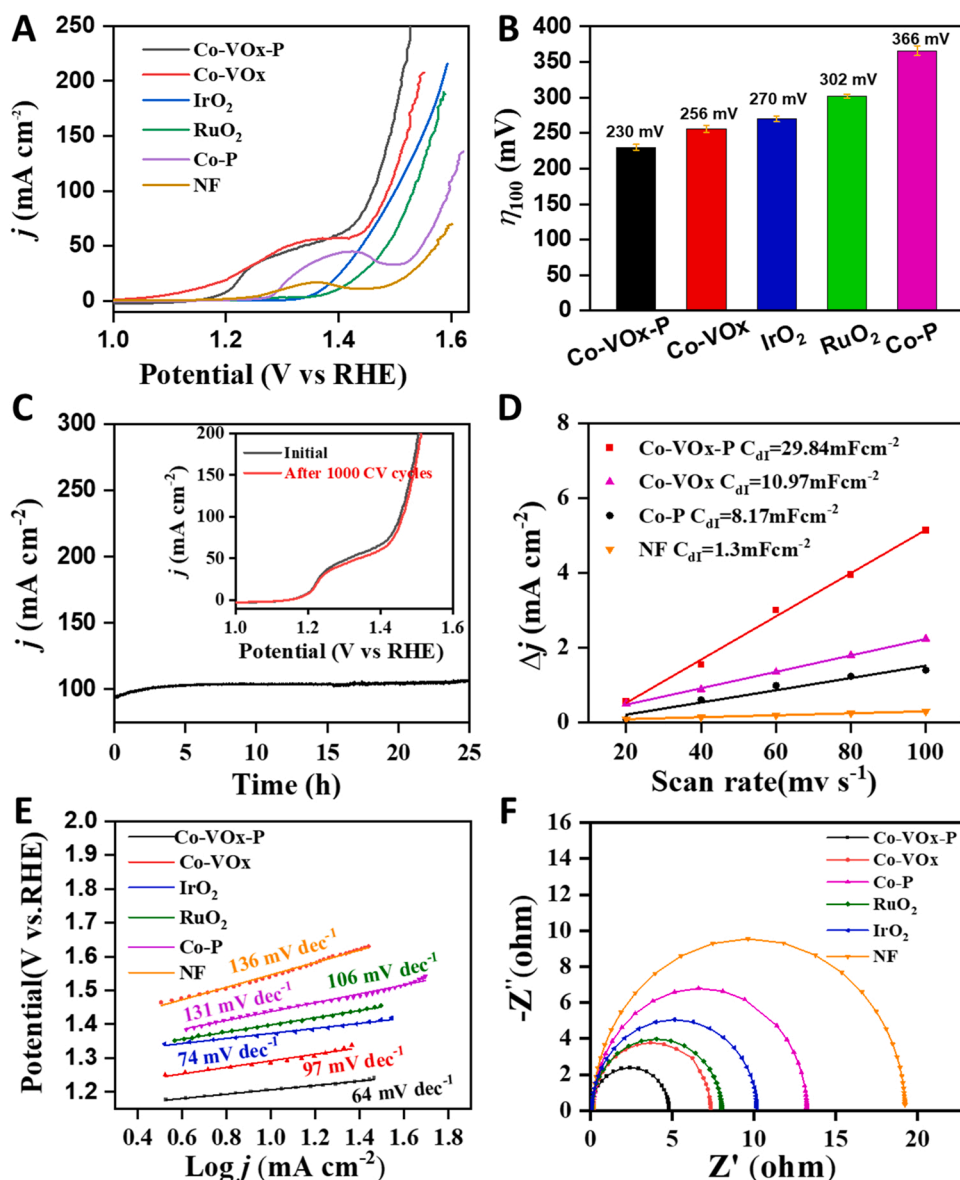


**Fig. 4.** Electrochemical measurements. (A) OER polarization curves of Co-VOx-P, Co-VOx, Co-P, bare Ni foam (NF), commercial IrO<sub>2</sub> and commercial RuO<sub>2</sub> catalysts in 1.0 M KOH. (B) The comparison of overpotential for delivering 100 mA/cm<sup>2</sup> OER current density. (C) Stability test of Co-VOx-P catalyst through the method of successive potential cycling and long-term operation. (D) C<sub>dl</sub> of the Co-VOx-P, Co-VOx, Co-P and NF. (E) Tafel slopes of Co-VOx-P, Co-VOx, Co-P and NF. (F) EIS spectra of Co-VOx-P, Co-VOx, Co-P and NF.

catalysts. The broad peak in the range of 1.2–1.4 V should be the oxidation of Co/Ni at high valence states [42]. We chose a large current density to evaluate the catalysis. For the current density of 100 mA/cm<sup>2</sup>, Co-VOx-P required only an overpotential of 230 mV, 136 mV less than that one of Co-P (366 mV) and 26 mV less than Co-VOx (256 mV) (Fig. 4B). Co-VOx-P also shows better catalytic performance than commercial IrO<sub>2</sub>, RuO<sub>2</sub>, and the recently reported NiVr-LDH catalyst (247 mV) and NiFeV catalyst (264 mV) [43]. To our knowledge, the present Co-VOx-P manifests the best of Co-based catalyst reported till now. This advantage for oxygen evolution became more remarkable in high current density range. With the increase of overpotential, the current density of Co-VOx-P increased more sharply in contrast to the other electrocatalysts. The durability property was evaluated with repeated potential cycling in the potential range of OER polarization. Co-VOx-P performed stable OER performances after 1000 times of potential cycles (Fig. 4C), the OER polarization curve almost overlaps with the initial one. The durability was then evaluated by a long-term chronoamperometry test at an overpotential of 230 mV. It is interesting that the current density increased slowly and reach 110 mA/cm<sup>2</sup> after 25 h. The slight increase of the OER electrolysis current density also appeared in other V contained electrocatalysts [28].

To understand the profound reason for the enhanced OER performance, the electrochemical active area was obtained from C<sub>dl</sub> calculated by the CV curves with different sweeping speeds. In the OER condition, Co-VOx-P still showed the highest EASA, three times larger than that one of Co-P (Fig. 4D). However, the current improvement is far more than three times, with an overpotential of 300 mV, Co-VOx-P delivered a current density of 270 mA/cm<sup>2</sup>, nearly seven times higher than that one of Co-P (39 mA/cm<sup>2</sup>). The difference between the active area and current density suggested that the performance enhancement might partly be attributed to the increased active area. To reveal the competitive advantage of intrinsic activity, Tafel slopes in the OER process were analyzed. Co-VOx-P displayed the lowest Tafel slope of 64 mV dec<sup>-1</sup>, indicating the advantage in intrinsic catalytic activity of catalytic sites (Fig. 4E). EIS was carried out to seek the reason for the high intrinsic catalytic activity of Co-VOx-P from the conductivity. The Nyquist profiles of all the electrodes show distinct semicircles with different diameters at the high-frequency regions, relative to the difference in charge transfer capacity (Fig. 4F). The semicircle of Co-VOx-P showed the smallest diameter, suggesting the lowest resistance for charge transfer, that is, the highest conductivity, which is in agreement with the Tafel slopes data. The present Co-VOx-P was also compared with the

recently reported OER electrocatalysts (Table 2). Considering the above electrochemical results, the present Co-VOx-P catalysts are efficient in catalytic water electrolysis (Fig. S17).

The structure of the catalyst after OER durability test was determined (Fig. S18–S22). There is no obvious change in morphologies and crystallization. The peaks at  $41.02^\circ$ ,  $41.78^\circ$  and  $48.96^\circ$  relative to the planes of (112), (210) and (013) for  $\text{Co}_2\text{P}$  slightly enhanced after durability test (Fig. S18). The flower-like structure still preserved but the contents of Co and V decreased slightly might be due to the long-time operation at high potential (Fig. S19). However, the elements of Co, P, O and V still distributed uniformly in micro-scale (Fig. S20). TEM image showed that the catalyst was still composed of many tiny nanoparticles with distinct lattices of  $\text{Co}_2\text{P}$  (Fig. S21). The uniform elemental distribution was also evaluated by TEM-EDS mapping and line scanning (Fig. S22).

### 3.4. DFT analysis

The above results indicate that compositional and structural add-in merits of Co-VOx-P surface contribute synergistically to enhanced catalytic activities for electrochemical water splitting. Generally, based on Sabatier's principle, too strong or too weak interaction between the catalysts surface and the reaction intermediates shows inverse effects to the catalytic reactions. The incorporation of V atoms might downshift the *d*-band position of Co-P, weakening the adsorption strength. Meanwhile, the relatively stronger interaction between OH and VOx might further weaken the chemisorption of oxygen-containing intermediates on the adjacent metal atoms and accelerate the electrocatalytic kinetics. We here also performed a DFT calculation to shed light on the enhanced catalytic activities of Co-Vox-P catalyst as compared to Co-P. The Gibbs free energy for each elementary step and the overpotential for electrode reactions were calculated and analyzed. Our calculation was focused on the enhanced activity on Co atoms after V incorporation. The stability evaluation of Co-Vox-P and the geometry/electronic structures optimization were performed in the Vienna Ab-initio Simulation Package (VASP) according to the experimental analysis of XRD, XPS and TEM characterizations [34,35]. For Co-P, a three-layer (111) surface was used. For Co-Vox-P material, a four-layer of  $3 \times 3$  supercell of (101)

surface was built (Figs. 5A, B).

The overall OER in an alkaline media can be described as  $4\text{OH}^- \rightarrow \text{O}_2 + 4\text{e}^- + 2\text{H}_2\text{O}$ . The HER in alkaline environment can be described as  $2\text{e}^- + 2\text{H}_2\text{O} \rightarrow \text{H}_2 + 2\text{OH}^-$ . Each of the above overall process can be divided into several elementary steps as shown in Fig. 5 and Fig. 6. The configurations of the intermediates on Co-VOx-P and Co-P surfaces were illustrated in Fig. 5. The reaction Gibbs free energy changes ( $\Delta G$ ) for each elementary step were calculated and used as a descriptor for the theoretical overpotentials.

The OER steps are generally recognized to carry out on the active transition metal sites (Co), the intermediates of  $\ast\text{OH}$ ,  $\ast\text{O}$  and  $\ast\text{OOH}$  bond to the catalytic sites with a single oxygen-bond and undergo a  $4\text{e}^-$ -process. Firstly, hydroxide anion ( $\text{OH}^-$ ) adsorbs on the catalytic sites ( $\ast$ ) and transfers to Co-OH ( $\ast\text{OH}$ ) via one-electron oxidation. Secondly, Co-OH transforms into Co-O ( $\ast\text{O}$ ) through a removal of a proton and one-electron. Subsequently, Co-O converts to Co-OOH ( $\ast\text{OOH}$ ) after combining with a hydroxyl anion with one-electron oxidation. Finally, oxygen molecular is generated and released after another proton-coupled one-electron removal step. The reaction Gibbs free energy of each elemental step is calculated by deviating the adsorption energy of the two adjacent intermediates. Thus, the corresponding rate-determining is assigned to the elementary step with the largest free energy [45]. The interaction strength between the catalytic active sites and the reaction intermediates (OH, O and OOH) determines the kinetics of OER. The Gibbs free bond energy of each intermediate was reflected in the free energy diagram and Table S3. For the OER, due to the strong interaction between Co-P surface and oxygen-containing intermediates, the formation of  $\ast\text{OH}$  releases energy and the  $\ast\text{OH}$  locates at the bottom of the energy diagram, indicating a requirement of more energy adsorption in the following steps to achieve the final free energy (Fig. 5C). In addition, the strong adsorption of oxygen on the catalytic sites will make the formation of Co-OOH more difficult [46]. Thus, the maximum  $\Delta G$  for OER on Co-P is from  $\ast\text{O}$  to  $\ast\text{OOH}$  (1.34 eV), and the  $\eta$  is calculated to be 0.94 V. On the Co-Vox-P surface, the chemisorption of oxygen-containing intermediates on the metal atoms is greatly weakened by V incorporation. The free energy for each intermediate on Co-VOx-P changed accordingly (Table S3). Despite the maximum  $\Delta G$  for

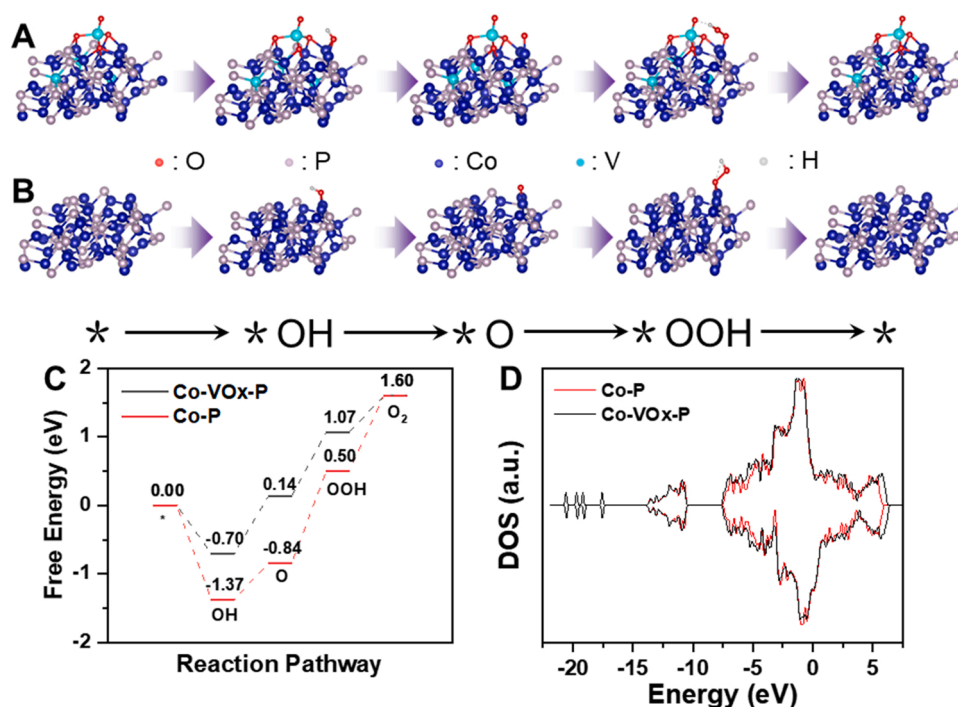


**Fig. 5.** The optimized interaction between intermediates on (A) Co-VOx-P and (B) Co-P surfaces for the OER process. (C) The Free Energy diagram for each elemental step of OER for Co-VOx-P and Co-P. (D) Total Density of states (DOSs) of Co-VOx-P and Co-P. (O: red, P: pink, V: cyan, Co: blue, H: gray).



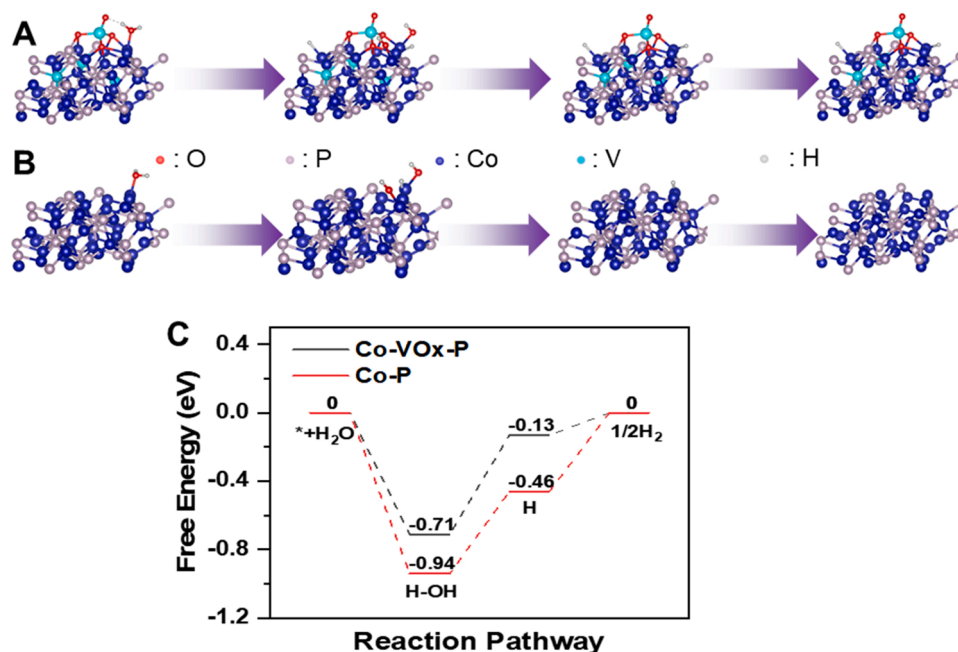


**Fig. 6.** The optimized interaction between intermediates on (A) Co-VOx-P and (B) Co-P surfaces for the HER process. (C) The Free Energy diagram for each elemental step of HER for Co-VOx-P and Co-P. (O: red, P: pink, V: cyan, Co: blue, H: gray).

OER on Co-VOx-P is still the step from  $^*O$  to  $^*OOH$  (0.93 eV), the  $\eta$  is calculated to be only 0.53 V, 0.39 V lower than that of Co-P surface.

To gain a further insight to the effect of V, the electronic states of Co-VOx-P and Co-P were also analyzed through DFT calculation (Fig. S23-S25). As presented in the profiles of the total densities of states (DOS) and the projected densities of states, the  $d$ -center of Co-P and Co-VOx-P is  $-1.244$  eV and  $-1.271$  eV, respectively, indicating the great influence of V incorporation and the change in surface adsorption properties (Fig. 5D). It has been well acknowledged that the deeper  $d$ -band center normally result in a weaker binding strength between intermediates and catalyst surface [47,48]. In our work, the  $d$ -center of Co-VOx-P is  $-1.271$  eV, deeper than that of Co-P ( $-1.244$ ), suggesting a weaker intermediate's binding strength, which is in consistence with free energy calculation results.

Despite a two-electron process, the HER still shows complexity and unclarity in alkaline (Figs. 6A, B) [43]. Generally, the HER includes water adsorbing on catalytic sites, water dissociating,  $OH^-$  desorbing, hydrogen recombining and releasing. Firstly, adsorbed water molecular on active sites transfers to adsorbed hydroxyl ion and Co-H ( $^*H$ ) after one-electron acceptance. The absorbed energy for this step is mainly used for water dissociation. The adsorbed hydroxyl ion then releases without electron transfer. Finally, adsorbed hydrogen ( $^*H$ ) recombine and release after another electron transfer process.

The reaction free energy profile for HER in alkaline was drawn as a diagram in Fig. 6C. Comparing with Co-P, the barriers for water adsorption, water dissociation to form adsorbed Co-H ( $^*H$ ), the combination of  $^*H$  with a proton from adjacent water molecular to form adsorbed  $H_2$  and  $H_2$  release are greatly reduced after V modification. It has been recognized that an efficient electrocatalyst should present the bonding energy of each intermediate close to zero [49]. Especially, the H adsorption free energy, a commonly used descriptor for HER, on the Co-Vox-P is  $-0.71$  eV, much weaker than that on Co-P surface ( $-0.94$  eV), indicating that the desorption of  $^*H$  and  $H_2$  production is more thermodynamically favorable. As to the HER under alkaline environmental, the dissociation of water is recognized as a critical rate-determining step because that hydrogen is originated from water [50]. The energy barrier corresponding to the HO-H bond breaking on Co-P is reflected as  $-0.46$  eV, in contrast, the dissociation energy on

Co-Vox-P surface is reduced to  $-0.13$  eV. Thus, the Co-Vox-P surface can accelerate water dissociation and promote the formation of  $^*H$  by orders of magnitude.

#### 4. Conclusion

In summary, a self-supported Co-VOx-P catalyst on Ni foam is developed for efficient and stable alkaline water splitting. Electrochemical measurements show that the excellent catalytic performances are partially attributed to the increased electrochemical active area, and mainly ascribed to the enhanced intrinsic catalytic activity and conductivity. Structural analysis and theory calculation showed that the combination of vanadium and phosphorus can modify the surface electronic state, tune the adsorption properties between intermediates and catalytic sites, which can substantially lower the overpotentials for both hydrogen evolution and oxygen evolution. Our work demonstrates that the combination of electrophilic element and metalloids with high valence states might be an effective strategy for the developing of excellent transition metal based electrocatalysts for water electrolysis.

#### Supporting Information

The supporting information includes: detailed experimental procedures and all other controlled samples. Additional TEM images, electrochemical measurements, etc.

#### CRediT authorship contribution statement

**Tao Yang:** Conceptualization, Methodology, Formal analysis, Writing – review & editing, Resources, Supervision, Project administration, Funding acquisition. **Zizheng Zhu:** Methodology, Validation, Investigation. **Kai Xu:** Methodology, Validation, Investigation. **Wen Guo:** Methodology, Validation, Investigation. **Hongyan Zhang:** Methodology, Validation, Investigation. **Xin Xiao:** Methodology, Validation, Investigation. **Maoshuai He:** Conceptualization, Methodology, Resources, Supervision, Project administration. **Tingting Yu:** Methodology, Validation, Formal analysis. **Hong Zhao:** Methodology, Validation, Formal analysis. **Donggen Zhang:** Conceptualization, Methodology.



## Declaration of Competing Interest

The authors declare no competing financial interest.

## Acknowledgment

This work was financially supported by the Six Talent Peaks Project of Jiangsu Province (XCL-004), the Key Project of “HaiYan” Program of Lianyungang (No. 2017-ZD-004), the Natural Science Foundation of Jiangsu Province (No. BK20201466 and BK20181074), the China Postdoctoral Science Foundation (2021M691327), the Jiangsu Postdoctoral Science Foundation (2021K313C), the Postgraduate Research & Practice Innovation Program of Jiangsu Province (KYCX20\_2921, KYCX20\_2919, KYCX21\_3138), the Key University Science Research Project of Jiangsu Province (No. 19KJA430007), and the project funded by the Priority Academic Program Development of Jiangsu Higher Education Institutions (PAPD).

## Appendix A. Supporting information

Supplementary data associated with this article can be found in the online version at [doi:10.1016/j.apcatb.2021.120985](https://doi.org/10.1016/j.apcatb.2021.120985).

## References

- [1] H.A. Gasteiger, N.M. Marković, Just a dream—or future reality? *Science* 324 (2009) 48–49.
- [2] J. Mohammed-Ibrahim, X. Sun, Recent progress on earth abundant electrocatalysts for hydrogen evolution reaction (HER) in alkaline medium to achieve efficient water splitting – a review, *J. Energy Chem.* 34 (2019) 111–160.
- [3] D.R. Gamelin, Water splitting: catalyst or spectator? *Nat. Chem.* 4 (2012) 965–967.
- [4] N.-T. Suen, S.-F. Hung, Q. Quan, N. Zhang, Y.-J. Xu, H.M. Chen, Electrocatalysis for the oxygen evolution reaction: recent development and future perspectives, *Chem. Soc. Rev.* 46 (2017) 337–365.
- [5] X. Zou, Y. Zhang, Noble metal-free hydrogen evolution catalysts for water splitting, *Chem. Soc. Rev.* 44 (2015) 5148–5180.
- [6] T.-J. Wang, H.-Y. Sun, Q. Xue, M.-J. Zhong, F.-M. Li, X. Tian, P. Chen, S.-B. Yin, Y. Chen, Holey platinum nanotubes for ethanol electrochemical reforming in aqueous solution, *Sci. Bull.* 66 (2021) 2079–2089.
- [7] W. Song, M. Li, C. Wang, X. Lu, Electronic modulation and interface engineering of electrospun nanomaterials-based electrocatalysts toward water splitting, *Carbon Energy* 3 (2021) 101–128.
- [8] Q. Shi, C. Zhu, D. Du, Y. Lin, Robust noble metal-based electrocatalysts for oxygen evolution reaction, *Chem. Soc. Rev.* 48 (2019) 3181–3192.
- [9] Y. Jiao, Y. Zheng, M. Jaroniec, S.Z. Qiao, Design of electrocatalysts for oxygen- and hydrogen-involving energy conversion reactions, *Chem. Soc. Rev.* 44 (2015) 2060–2086.
- [10] T. Zhao, Y. Wang, S. Karuturi, K. Catchpole, Q. Zhang, C. Zhao, Design and operando/in situ characterization of precious-metal-free electrocatalysts for alkaline water splitting, *Carbon Energy* 2 (2020) 582–613.
- [11] X. Qin, D. Kim, Y. Piao, Metal-organic frameworks-derived novel nanostructured electrocatalysts for oxygen evolution reaction, *Carbon Energy* 3 (2021) 66–100.
- [12] J. Xu, Y. Liu, J. Li, I. Amorim, B. Zhang, D. Xiong, N. Zhang, S.M. Thalluri, J.P. S. Sousa, L. Liu, Hollow cobalt phosphide octahedral pre-catalysts with exceptionally high intrinsic catalytic activity for electro-oxidation of water and methanol, *J. Mater. Chem. A* 6 (2018) 20646–20652.
- [13] Z. Xiao, Y. Wang, Y.-C. Huang, Z. Wei, C.-L. Dong, J. Ma, S. Shen, Y. Li, S. Wang, Filling the oxygen vacancies in  $\text{Co}_3\text{O}_4$  with phosphorus: an ultra-efficient electrocatalyst for overall water splitting, *Energy Environ. Sci.* 10 (2017) 2563–2569.
- [14] E.J. Popczun, C.G. Read, C.W. Roske, N.S. Lewis, R.E. Schaak, Highly active electrocatalysis of the hydrogen evolution reaction by cobalt phosphide nanoparticles, *Angew. Chem. Int. Ed.* 53 (2014) 5427–5430.
- [15] A. Mendoza-Garcia, H. Zhu, Y. Yu, Q. Li, L. Zhou, D. Su, M.J. Kramer, S. Sun, Controlled anisotropic growth of Co-Fe-P from Co-Fe-O nanoparticles, *Angew. Chem. Int. Ed.* 54 (2015) 9642–9645.
- [16] J. Xu, J. Li, D. Xiong, B. Zhang, Y. Liu, K.-H. Wu, I. Amorim, W. Li, L. Liu, Trends in activity for the oxygen evolution reaction on transition metal (M = Fe, Co, Ni) phosphide pre-catalysts, *Chem. Sci.* 9 (2018) 3470–3476.
- [17] W. Zhang, Y. Sun, Q. Liu, J. Guo, X. Zhang, Vanadium and nitrogen co-doped CoP nanoleaf array as pH-universal electrocatalyst for efficient hydrogen evolution, *J. Alloy. Comp.* 791 (2019) 1070–1078.
- [18] C. Tang, R. Zhang, W. Lu, L. He, X. Jiang, A.M. Asiri, X. Sun, Fe-doped CoP nanoarray: a monolithic multifunctional catalyst for highly efficient hydrogen generation, *Adv. Mater.* 29 (2017) 1602441.
- [19] W. Li, X. Gao, D. Xiong, F. Xia, J. Liu, W.-G. Song, J. Xu, S.M. Thalluri, M. F. Cerveira, X. Fu, L. Liu, Vapor–solid synthesis of monolithic single-crystalline CoP nanowire electrodes for efficient and robust water electrolysis, *Chem. Sci.* 8 (2017) 2952–2958.
- [20] H. Huang, C. Yu, C. Zhao, X. Han, J. Yang, Z. Liu, S. Li, M. Zhang, J. Qiu, Iron-tuned super nickel phosphide microstructures with high activity for electrochemical overall water splitting, *Nano Energy* 34 (2017) 472–480.
- [21] B. You, N. Jiang, M. Sheng, M.W. Bhusan, Y. Sun, Hierarchically porous urchin-like  $\text{Ni}_2\text{P}$  superstructures supported on nickel foam as efficient bifunctional electrocatalysts for overall water splitting, *ACS Catal.* 6 (2016) 714–721.
- [22] L. Yin, X. Ding, W. Wei, Y. Wang, Z. Zhu, K. Xu, Z. Zhao, H. Zhao, T. Yu, T. Yang, Improving catalysis for electrochemical water splitting using a phosphosulphide surface, *Inorg. Chem. Front.* 7 (2020) 2388–2395.
- [23] M. Cabán-Acevedo, M.L. Stone, J.R. Schmidt, J.G. Thomas, Q. Ding, H.-C. Chang, M.-L. Tsai, J.-H. He, S. Jin, Efficient hydrogen evolution catalysis using ternary pyrite-type cobalt phosphosulphide, *Nat. Mater.* 14 (2015) 1245–1253.
- [24] W. Liu, E. Hu, H. Jiang, Y. Xiang, Z. Weng, M. Li, Q. Fan, X. Yu, E.I. Altman, H. Wang, A highly active and stable hydrogen evolution catalyst based on pyrite-structured cobalt phosphosulfide, *Nat. Commun.* 7 (2016) 10771.
- [25] Y. Qu, M. Shao, Y. Shao, M. Yang, J. Xu, C.T. Kwok, X. Shi, Z. Lu, H. Pan, Ultra-high electrocatalytic activity of  $\text{VS}_2$  nanoflowers for efficient hydrogen evolution reaction, *J. Mater. Chem. A* 5 (2017) 15080–15086.
- [26] X. Peng, L. Hu, L. Wang, X. Zhang, J. Fu, K. Huo, L.Y.S. Lee, K.-Y. Wong, P.K. Chu, Vanadium carbide nanoparticles encapsulated in graphitic carbon network nanosheets: a high-efficiency electrocatalyst for hydrogen evolution reaction, *Nano Energy* 26 (2016) 603–609.
- [27] X. Chen, K. Yu, Y. Shen, Y. Feng, Z. Zhu, Synergistic effect of  $\text{MoS}_2$  nanosheets and  $\text{VS}_2$  for the hydrogen evolution reaction with enhanced humidity-sensing performance, *ACS Appl. Mater. Interfaces* 9 (2017) 42139–42148.
- [28] K. Fan, H. Chen, Y. Ji, H. Huang, P.M. Claesson, Q. Daniel, B. Philippe, H. Rensmo, F. Li, Y. Luo, L. Sun, Nickel–vanadium monolayer double hydroxide for efficient electrochemical water oxidation, *Nat. Commun.* 7 (2016) 11981.
- [29] P. Li, X. Duan, Y. Kuang, Y. Li, G. Zhang, W. Liu, X. Sun, Tuning electronic structure of NiFe layered double hydroxides with vanadium doping toward high efficient electrocatalytic water oxidation, *Adv. Energy Mater.* 8 (2018) 1703341.
- [30] L. Liardet, X. Hu, Amorphous cobalt vanadium oxide as a highly active electrocatalyst for oxygen evolution, *ACS Catal.* 8 (2018) 644–650.
- [31] Y. Cui, Y. Xue, R. Zhang, J. Zhang, X. Li, X. Zhu, Vanadium–cobalt oxyhydroxide shows ultralow overpotential for the oxygen evolution reaction, *J. Mater. Chem. A* 7 (2019) 21911–21917.
- [32] J. Bao, Z. Wang, J. Xie, L. Xu, F. Lei, M. Guan, Y. Zhao, Y. Huang, H. Li, A ternary cobalt–molybdenum–vanadium layered double hydroxide nanosheet array as an efficient bifunctional electrocatalyst for overall water splitting, *Chem. Commun.* 55 (2019) 3521–3524.
- [33] J.-F. Qin, J.-H. Lin, T.-S. Chen, D.-P. Liu, J.-Y. Xie, B.-Y. Guo, L. Wang, Y.-M. Chai, B. Dong, Facile synthesis of V-doped CoP nanoparticles as bifunctional electrocatalyst for efficient water splitting, *J. Energy Chem.* 39 (2019) 182–187.
- [34] G. Kresse, J. Furthmüller, Efficient iterative schemes for ab initio total-energy calculations using a plane-wave basis set, *Phys. Rev. B* 54 (1996) 11169–11186.
- [35] G. Kresse, J. Furthmüller, Efficiency of ab-initio total energy calculations for metals and semiconductors using a plane-wave basis set, *Comput. Mater. Sci.* 6 (1996) 15–50.
- [36] J.P. Perdew, K. Burke, M. Ernzerhof, Generalized gradient approximation made simple, *Phys. Rev. Lett.* 77 (1996) 3865–3868.
- [37] J.P. Perdew, M. Ernzerhof, K. Burke, Rationale for mixing exact exchange with density functional approximations, *J. Chem. Phys.* 105 (1996) 9982–9985.
- [38] S. Grimme, Semiempirical GGA-type density functional constructed with a long-range dispersion correction, *J. Comput. Chem.* 27 (2006) 1787–1799.
- [39] K. Fan, H. Chen, Y. Ji, H. Huang, P.M. Claesson, Q. Daniel, B. Philippe, H. Rensmo, F. Li, Y. Luo, L. Sun, Nickel–vanadium monolayer double hydroxide for efficient electrochemical water oxidation, *Nat. Commun.* 7 (2016) 11981.
- [40] K. Fan, Y. Ji, H. Zou, J. Zhang, B. Zhu, H. Chen, Q. Daniel, Y. Luo, J. Yu, L. Sun, Hollow iron–vanadium composite spheres: a highly efficient iron-based water oxidation electrocatalyst without the need for nickel or cobalt, *Angew. Chem. Int. Ed.* 56 (2017) 3289–3293.
- [41] Y. Li, X. Tan, R.K. Hocking, X. Bo, H. Ren, B. Johannessen, S.C. Smith, C. Zhao, Implanting Ni-O-VOx sites into Cu-doped Ni for low-overpotential alkaline hydrogen evolution, *Nat. Commun.* 11 (2020) 2720.
- [42] J. Jiang, F. Sun, S. Zhou, W. Hu, H. Zhang, J. Dong, Z. Jiang, J. Zhao, J. Li, W. Yan, M. Wang, Atomic-level insight into super-efficient electrocatalytic oxygen evolution on iron and vanadium co-doped nickel (oxy)hydroxide, *Nat. Commun.* 9 (2018) 2885.
- [43] D. Wang, Q. Li, C. Han, Q. Lu, Z. Xing, X. Yang, Atomic and electronic modulation of self-supported nickel–vanadium layered double hydroxide to accelerate water splitting kinetics, *Nat. Commun.* 10 (2019) 3899.
- [44] T. Shinagawa, A.T. Garcia-Esparza, K. Takanabe, Insight on Tafel slopes from a microkinetic analysis of aqueous electrocatalysis for energy conversion, *Sci. Rep.* 5 (2015) 13801.
- [45] C. Hu, L. Zhang, J. Gong, Recent progress made in the mechanism comprehension and design of electrocatalysts for alkaline water splitting, *Energy Environ. Sci.* 12 (2019) 2620–2645.
- [46] Á. Valdés, J. Brillet, M. Grätzel, H. Gudmundsdóttir, H.A. Hansen, H. Jónsson, P. Klüpfel, G.-J. Kroes, F. Le Formal, I.C. Man, R.S. Martins, J.K. Nørskov, J. Rossmeisl, K. Sivula, A. Vojvodin, M. Zäch, Solar hydrogen production with semiconductor metal oxides: new directions in experiment and theory, *Phys. Chem. Chem. Phys.* 14 (2012) 49–70.

- [47] G.-P. Gao, S.-H. Wei, X. Gu, X.-M. Duan, Catalytic role of pre-adsorbed CO in platinum-based catalysts: the reduction of SO<sub>2</sub> by CO on Pt/Au(CO)<sub>n</sub>, *Phys. Chem. Chem. Phys.* 15 (2013) 12846–12851.
- [48] G. Gao, E.R. Waclawik, A. Du, Computational screening of two-dimensional coordination polymers as efficient catalysts for oxygen evolution and reduction reaction, *J. Catal.* 352 (2017) 579–585.
- [49] Y. Zheng, Y. Jiao, Y. Zhu, L.H. Li, Y. Han, Y. Chen, M. Jaroniec, S.-Z. Qiao, High electrocatalytic hydrogen evolution activity of an anomalous ruthenium catalyst, *J. Am. Chem. Soc.* 138 (2016) 16174–16181.
- [50] P. Wang, X. Zhang, J. Zhang, S. Wan, S. Guo, G. Lu, J. Yao, X. Huang, Precise tuning in platinum-nickel/nickel sulfide interface nanowires for synergistic hydrogen evolution catalysis, *Nat. Commun.* 8 (2017) 14580.